Pathogenic and transcriptomic differences of emerging SARS-CoV-2 variants in the Syrian golden hamster model — Source link ⧉

Kyle L. O'Donnell, Amanda N. Pinski, Chad S Clancy, Tylisha Gourdine ...+4 more authors

Institutions: National Institutes of Health, University of California, Irvine

Related papers:

- Comparing infectivity and virulence of emerging SARS-CoV-2 variants in Syrian hamsters.

- Comparative infectivity and pathogenesis of emerging SARS-CoV-2 variants in Syrian hamsters

- SARS-CoV-2 variants reveal features critical for replication in primary human cells.

- Emerging SARS-CoV-2 Variants and Impact in Global Vaccination Programs against SARS-CoV-2/COVID-19.

- Rescue of SARS-CoV-2 from a single bacterial artificial chromosome

Share this paper: 📘 🐦 in ✉

View more about this paper here: https://typeset.io/papers/pathogenic-and-transcriptomic-differences-of-emerging-sars-4x9xnrntuc

1   **Pathogenic and transcriptomic differences of emerging SARS-CoV-2 variants in**

2   **the Syrian golden hamster model**

3

4   Kyle L. O'Donnell[1#], Amanda N. Pinski[2#], Chad S. Clancy[3], Tylisha Gourdine[1], Kyle Shifflett[1], Paige

5   Fletcher[1], Ilhem Messaoudi[2], and Andrea Marzi[1]*

6

7   [1]Laboratory of Virology, Division of Intramural Research, National Institute of Allergy and

8   Infectious Diseases, National Institutes of Health, Hamilton, MT 59840, USA

9   [2]Department of Molecular Biology and Biochemistry, University of California, Irvine, Irvine, CA

10   92697, USA

11   [3]Rocky Mountain Veterinary Branch, Division of Intramural Research, National Institute of

12   Allergy and Infectious Diseases, National Institutes of Health, Hamilton, MT 59840, USA

13

14   #authors contributed equally

15

16   *corresponding author

17   Andrea Marzi

18   marzia@niaid.nih.gov

19

20

21 **Abstract**

22 Following the discovery of severe acute respiratory syndrome coronavirus 2 (SARS-CoV-2) and

23 its rapid spread throughout the world, new viral variants of concern (VOC) have emerged. There

24 is a critical need to understand the impact of the emerging variants on host response and

25 disease dynamics to facilitate the development of vaccines and therapeutics. Syrian golden

26 hamsters are the leading small animal model that recapitulates key aspects of severe

27 coronavirus disease 2019 (COVID-19). In this study, we show that intranasal inoculation of

28 SARS-CoV-2 into hamsters with the ancestral virus (nCoV-WA1-2020) or VOC first identified in

29 the United Kingdom (B.1.1.7) and South Africa (B.1.351) led to similar gross and histopathologic

30 pulmonary lesions. Although differences in viral genomic copy numbers were noted in the lungs

31 and oral swabs of challenged animals, infectious titers in the lungs were comparable. Antibody

32 neutralization capacities varied, dependent on the original challenge virus and cross-variant

33 protective capacity. Transcriptional profiling indicated significant induction of antiviral

34 pathways in response to all three challenges with a more robust inflammatory signature in

35 response to B.1.1.7. Furthermore, no additional mutations in the spike protein were detected

36 at peak disease. In conclusion, the emerging VOC showed distinct humoral responses and

37 transcriptional profiles in the hamster model compared to the ancestral virus.

38

39

Introduction

44   Severe acute respiratory syndrome coronavirus-2 (SARS-CoV-2) has emerged as a novel, highly

45   infectious respiratory CoV and the causative agent of CoV disease 2019 (COVID-19)[1]. First

46   described in the city of Wuhan in Hubei province of China, SARS-CoV-2 is a member of the

47   *Coronavirdae* family, which possess large, non-segmented RNA genomes[1]. High levels of

48   transmission, especially in regions with low vaccination rates, facilitate the emergence of

49   mutations that improve viral fitness. SARS-CoV-2 variants of concern (VOC) are defined as

50   variants that have one or more mutations that confer worrisome epidemiologic, immunologic,

51   or pathogenic properties[2]. Several SARS-CoV-2 VOC have emerged such as B.1.1.7 first reported

52   in the United Kingdom (UK), which is associated with increased transmission compared to the

53   ancestral virus reported from Washington, USA in early 2020[3]. This variant acquired over 20

54   mutations including N501Y within the spike (S) protein that increased binding affinity to the

55   angiotensin converting enzyme 2 (ACE2) receptor[4,5]. In addition, the S protein of the B.1.1.7

56   variant has a deletion of amino acids 69 and 70 which has been shown to increase viral escape

57   in immunocompromised individuals[6,7]. VOC B.1.351 was originally reported in South Africa (SA)

58   and harbors similar mutations in S compared to B.1.1.7 as well as the K417N and E484K

59   substitutions that may decrease the efficacy of existing vaccines[8-12]. Other variants more

60   recently reported in the United States (B.1.427, B1.429) also harbor mutations in S (e.g., N501Y)

61   that have been associated with reductions in neutralizing antibody titers[13].

62

63   There is an urgent need to understand the effect of new mutations within VOC on the host

64   immune response to facilitate the development of vaccines and therapeutics. In this study, we

65   compared pathologic features of and immune responses to the original virus (ancestral), and

66   the later B.1.1.7 and B.1.351 variants in the well-established Syrian golden hamster model of

67   severe COVID-19[14]. Specifically, we longitudinally assessed viral replication, histopathological

68   changes, development of humoral immunity and humoral cross-reactivity amongst VOC.

69   Additionally, we employed RNA-seq and digital cell quantification of lung homogenates to

70   determine differences in transcriptomic signatures and to infer changes in immune cell subsets.

71   We identified similar histopathological changes, levels of infectious virus, and antibody titers

72   amongs all infections. However, transcriptional responses and the capacity to cross-neutralize

73   SARS-CoV-2 was VOC-dependent. Collectively, these data demonstrate that mutations within

74   SARS-CoV-2 modulate host defense pathways.

75

76   **Results**

77   *Gross lung pathology*

78   Syrian golden hamsters were separated into three cohorts (n=15 per cohort) and challenged

79   intranasally (IN) with 10^5 TCID$_{50}$ of one of three different SARS-CoV-2 variants: ancestral (nCoV-

80   WA1-2020), B.1.1.7, and B.135. Five uninfected animals served as negative controls. Scheduled

81   necropsies were performed at 4, 14, and 28 days post-challenge (DPC) for all groups to capture

82   peak disease and convalescence (Fig. S1A). Peak weight loss was achieved amongst all three

83   groups 7 DPC, however, no significant difference in body weight changes occurred over the first

84   10 DPC for any of the infections (Fig. S1B). Gross pulmonary lesions were observed in all

85   infected hamsters at 4 DPC (Fig. S1D). Lungs harvested 4 DPC showed multifocal to locally

86   extensive areas of red to purple coloration (consistent with consolidation) disseminated

87   throughout all lung lobes. Additionally, lungs generally failed to collapse indicating interstitial

88   disease. Lung samples harvested 14 and 28 DPC had either no gross lesions or limited, small,

89   multifocal areas of consolidation and/or congestion. Analysis of histopathology samples

90   demonstrated evidence of interstitial pneumonia on 4 and 14 DPC in all groups (Fig. S1C).

91

92   *Histopathology and immunohistochemistry of hamster lungs*

93   Pulmonary pathology consistent with previously described coronavirus respiratory disease was

94   observed at 4 DPC in lung samples from hamsters infected with each virus (Fig. 1)[15]. Five

95   uninfected animals served as negative controls (Fig. 1A, E, I). Foci of interstitial pneumonia and

96   bronchiolitis were observed throughout all evaluated lung lobes of infected hamsters. Minimal

97   to mild bronchiolitis characterized by individual epithelial cell necrosis, epithelial cell basophilia

98   and hyperplasia and rare syncytial cell formation was observed throughout all variants (Fig. 1 B-

99   D). Interstitial pneumonia varying in percent of lung involvement and moderate to severe

100   severity was observed within each animal regardless of the variant. Interstitial pneumonia at 4

101   DPC was defined by expansion of alveolar septa by edema fluid, leukocyte infiltration and fibrin,

102   with leukocyte spillover into adjacent alveolar spaces and in severe cases, complete loss of

103   pulmonary architecture (Fig. 1 F-H). Tracheitis characterized by neutrophilic influx and epithelial

104   cell necrosis was observed in all evaluated sections of trachea in each animal at 4 DPC.

105   Immunohistochemical analysis showed immunoreactivity to an antibody specific to SARS-CoV-2

106   within bronchiolar epithelia, type I and type II pneumocytes and macrophages in lungs of all

107   hamsters regardless of the viral variant (Fig. 1 J-L).

108   At 14 and 28 DPC pulmonary pathology was similar in lungs of hamsters infected with all viruses

109   (Fig. S1C, D). Foci of persistent type II pneumocyte hyperplasia with occasional apical cilia

110   formation (alveolar bronchiolization) adjacent to terminal bronchioles was observed

111   throughout all lung lobes. Frequently, foci of alveolar bronchiolization entrapped low to

112   moderate numbers of foamy macrophages. Antigen was not detected by immunohistochemical

113   evaluation for any viral variant at either 14 or 28 DPC.

114

115   *Viral burden*

116   Total viral RNA copy numbers and infectious viral titers were quantified in lungs of challenged

117   animals at the three time points mentioned above (Fig. 2A-C). There was no difference in viral

118   RNA copy numbers amongst challenged groups at 4 DPC (Fig. 2A). However, there was

119   significantly more viral RNA at 14 DPC in the B.1.1.7-challenged group compared to the

120   ancestral and B.1.351 groups. At 28 DPC there were significantly more viral RNA copies in the

121   lungs of ancestral-challenged hamsters than the B.1.1.7 group (Fig. 2A). We also assessed sub-

122   genomic viral RNA (sgRNA) as a surrogate of active viral replication[16,17]. Levels of lung sgRNA

123   peaked at 4 DPC and were comparable among the three variants (Fig. 2B). In contrast, we

124   observed a significant difference in sgRNA among the groups at 14 DPC. Specifically, B.1.1.7-

125   infected hamsters exhibited the highest residual sgRNA present compared to the ancestral and

126   B.1.351 groups (Fig. 2B). The B.1.351 group also had significantly higher sgRNA levels compared

127   to the ancestral group (Fig. 2B). However, infectious viral titers were only detected 4 DPC in

128   lungs in all hamsters (Fig. 2C).

129   Oral viral shedding and viremia were evaluated at the time of necropsy. Infection with the

130   B.1.1.7 VOC resulted in significantly more oral viral shedding than the B.1.351 variant at 4 and

131   14 DPC (Fig. 2D). Viremia peaked at 4 DPC and was comparable amongst all infections (Fig. 2E).

132   Profiling the viral genomes recovered from the lungs of infected hamsters at 4 DPC revealed no

133   changes in the viral sequences in ancestral and B.1.1.7-infected animals compared to the

134   reference genomes (Table 1). However, we identified three mutations in all B.1.351-infected

135   animals, including two nonsynonymous mutations in 5' UTR (T201C) and nsp3 (G172C), and one

136   synonymous mutation in nsp3 (G5942G). A single B.1.351-infected animal presented with an

137   additional mutation (L3892F) in nsp3 (Table 1). No mutations in S were detected.

138

139   *Humoral immune responses post-challenge*

140   We utilized standard ELISA methods to determine the SARS-CoV-2 S-specific IgG responses, and

141   S receptor-binding domain (RBD)-specific IgG responses. There was no difference in the S-

142   specific IgG titers at either 14 or 28 DPC amongst the groups (Fig. 3A). Similarly, no difference

143   was determined in the RBD-specific IgG titers at 14 DPC (Fig. 3B). However, at 28 DPC the RBD-

144   specific IgG titer was significantly higher in animals challenged with B.1.351 compared to

145   B.1.1.7 (Fig. 3B).

146   Next, we assessed the functionality of the humoral response by neutralization assay, not only

147   against the homologous challenge virus, but also against the other two variants to determine

148   cross-reactivity generated from the primary infection. Hamsters challenged with the ancestral

149   virus exhibited comparable neutralizing titers against the homologous challenge variant

150   (ancestral) and the B.1.1.7 variant at 14 and 28 DPC but lower titers against the B.1.351 variant

151   at both timepoints assessed (Fig. 3C). In contrast, hamsters challenged with the B.1.1.7 or the

152   B.1.351 variant each exhibited significantly higher neutralizing titers against their homologous

153   challenge virus at 14 DPC compared to variants to which they were not exposed (Fig.3D, E). This

154   difference persisted for the B.1.351-infected animals at 28 DPC when comparing anti-B.135.1

155   and anti-B.1.1.7 titers (Fig. 3E). Moreover, the overall neutralization titers against the B.1.351

156   variant were 1-2 logs lower than the other two variants regaradless of homolgous or

157   heterologous assessment.

158

159   *COVs elicit unique transcriptional responses in the lungs*

160   To elucidate differences in the host responses to VOC, we profiled the transcriptional responses

161   in lung tissues obtained at peak viral loads (4 DPC) (Fig. 4, S2). Principal component analysis

162   (PCA) revealed distinct separation between uninfected and uninfected animals (Fig. S2A), with

163   the B.1.1.7 variant infection resulting in the most distinct transcriptional profile and the largest

164   number of differentially expressed genes (DEGs) (n=1,277) while infection with B.1.351 resulted

165   in the smallest number of DEGs (n=395) (Fig. 4A-C). Most DEGs were upregulated following

166   infection with all three viruses (Fig. 4A-C). A core of 291 DEGs was shared by all variants and an

167   additional ~270 DEGs were shared only between B.1.1.7- and ancestral-infected hamsters (Fig.

168   4D).

169   We performed functional enrichment of DEGs in order to determine their biological relevance.

170   DEGs induced by all three viral infections enriched to Gene Ontology (GO) terms associated

171   with antiviral immunity (e.g., "response to virus"), immune cell recruitment (e.g., "leukocyte

172   chemotaxis") and mobilization of adaptive immunity (e.g., "lymphocyte activation", "B cell-

173   mediated immunity") (Fig. 4E). DEGs enriching to "response to virus" and common to all three

174   infections play roles in type I interferon (IFN) signaling (e.g., *IRF7, IRF9, STAT1/2*), nucleic acid

175   detection (e.g., *DDX60, DHX58*) and the antiviral response (e.g., *ISG15, MX1, RSAD2, SAMHD1*)

176   (Fig. S2B). These DEGs were upregulated following infection with all three variants, particularly

177   B.1.1.7. DEGs enriching to this GO term and upregulated following infection by the ancestral

178   and B.1.1.7 variants only were part of T cell activation pathways (e.g., *IFNG, IL12RB1, TBX21,*

179   *XCL1*) (Fig. S2B).

180   Other DEGs that were upregulated following infection with all three variants enriched to GO

181   term "blood vessel development". These genes are involved in angiogenesis (e.g., *ANGPTL2,*

182   *ANGPTL4, ADM2, HOX1*), apoptosis (e.g., *BAK1, FASLG*), tissue remodeling (e.g., *CHI3L1,*

183   *MMP19*), and leukocyte chemotaxis (e.g., *CCL11, CCL2, CXCL10, CXCL17*) (Fig. S2C). Regulators

184   of angiogenesis, like *SOX4* and *KDR*, and genes involved in tissue remodeling (e.g., ADAM12,

185   SHH) were downregulated only in infections with the B.1.1.7 and ancestral virus (Fig. S2C).

186   Shared DEGs that enriched to GO term "lymphocyte activation" included genes important for B

187   cell maturation (e.g., *AIRE, CD27, CD38, ICOS, TNFSF13B*) as well as negative regulation of T cell

188   responses (e.g., *CD274, CTLA4, FOXP3, IDO1, PDCDC1, PDCD1LG2*) (Fig. S2E). DEGs shared

189   between B.1.1.7- and ancestral-infected hamsters were important for T cell activation (e.g.,

190   *PRKCQ, TNFSF9*), cytotoxic responses (e.g., *KLRK1, PRF1*) myeloid cell activation (e.g., *IFNG,*

191   *SLAMF1, CD177, CXCL6*) and IL-6 production (e.g., *TLR1, IL-6, IL18RAP, C3AR1, C1QA*) (Fig. 4E,

192   S2D).

193   We next analyzed DEGs unique to each infection to understand infection-specific

194   transcriptional responses (Fig. 5). The largest group of unique DEGs was detected following

195   B.1.1.7 infection (n=648). These unique DEGs enriched to GO terms reflecting tissue remodeling

196   (e.g., "response to growth factor", "tissue morphogenesis") (Fig. 5A). Most DEGs in these GO

197   terms are downregulated and associated with angiogenesis (e.g., *ENG, JCAD, PDFGB, VEGFD*)

198   and lung development (e.g., *FZD1, SOX17, TMEM100, VANGL2*), while a smaller upregulated

199   portion was associated with cell death (e.g., *APAF1, CASP3*), and protein degradation (e.g.,

200   *CASP3, DAB2, SFRP1*). Other DEG enriched to GO terms associated with host defense (e.g.,

201   "adaptive immune response") and cell recruitment (e.g., "chemotaxis") were identified. Most of

202   these DEGs were upregulated and are important for antigen presentation (e.g., *CD74, HLA-DRA,*

203   *B2M*) and natural killer (NK) cell-mediated immunity (e.g., *CD84, IL12A*) (Fig. 5B-D). Notable

204   DEGs unique to infection with B.1.351 play a role in cell morphogenesis (e.g., *ACTA2, ACTC1,*

205   *FGF1*), myeloid cell differentiation (e.g., *CAV3, PDE1B, TFRC*), and response to injury (e.g.

206   *COL4A3, MPL, TSPAN*) (Fig. 5E). Downregulated DEGs unique to infection with the ancestral

207   strain encoded components of cellular respiration (e.g., *MT-C03, MT-ND1*) and mediators of cell

208   adhesion (e.g., *IKF26B, VIT*) (Fig. 5F).

209

210   *Digital cell quantification in hamster lungs*

211   Since Syrian golden hamsters lack adequate reagents for immunophenotyping, we performed

212   digital cell quantification (DCQ) to predict changes in immune cell populations using the IRIS

213   immune cell database[18]. Changes in gene expression were predicted to be associated with

214   increased frequencies of activated NK cells, activated dendritic cells (DCs), and neutrophils after

215   ancestral and B.1.1.7 infection (Fig. S3A). In contrast, B.1.351 infection was associated with a

216   decrease in NK cells and monocytes (Fig. S3B). Reduced frequencies of B cells were predicted

217   for all infections, while increases in Th1 and Th2 CD4+ T cells were only predicted after B.1.1.7

218   infection (Fig. S3B).

219

220   **Discussion**

221   Over the last several months a number of SARS-CoV-2 VOC have emerged. These VOC are

222   associated with increased transmissibility and enhanced viral fitness due to mutations in S.

223   Several studies have shown that the N501Y mutation harborded in both the B.1.1.7 and the

224   B.1.351 variants utilized here increases ACE2 binding and enhances transmission

225   capabilities[4,5,19]. The K417N and E484K mutations introduced into the S of the B.1.351 enhances

226   the ability to evade pre-existing humoral responses[3,7,10,20-22]. A comparative study of viral

227   pathogenesis of VOC has recently been conducted in the hamster model[23]. The study measured

228   the viral burden, histopathology, and select cytokine gene expression induced by VOC

229   compared to the prototypic Wuhan-Hu-1 isolate and an isolate harboring the secondary D614G

230   mutation in S. The study showed no significant differences in viral burden and histopathologic

231   findings in the hamster lungs at 4 DPC, but enhanced expression of cytokine genes was

232   described in hamsters infected with the B.1.1.7 variant.[23] However, longitudinal analysis of the

233   host response to VOC and the degree of cross-protection is lacking. Therefore, in this study, we

234   sought to evaluate the longitudinal impact of these VOC on the host immune and

235   transcriptional responses.

236   Syrian golden hamsters were chosen for this study as they are highly susceptible to infection

237   and were found to have high viral replication in the lungs. Hamsters were infected IN with the

238   ancestral, B.1.1.7 or B.1.351 variants. Challenged hamsters displayed moderate weight loss

239   lethargy, rapid breathing, and ruffled fur, but were able to clinically recover by 14 DPC as

240   previously described[14,24,25]. As recently reported, no discernable differences in gross pathology

241   or lung viral burden were noted among all three groups[26]. However, B.1.1.7 sgRNA persisted

242   longer in the hamster lungs. Analysis of the viral genomes recovered post-infection showed no

243   changes in the ancestral- and B.1.1.7-infected hamsters; however, we detected three mutations

244   in all B.1.351-infected animals. The two nonsynonymous mutations occurred in nsp3 and

9

245 ORF3a, both of which have been implicated in evasion of type I IFN[27,28]. A second mutation in

246 nsp3 was also identified in a single B.1.351-infected animal. The implication of these mutations

247 remains to be elucidated.

248 Analysis of the humoral response revealed that the overall IgG response of the infected

249 hamsters did not result in robust differences amongst the variants; however, the neutralization

250 cross-protection depended on the variant the hamster was initially exposed to. Specifically,

251 infection with B.1.1.7 results in the widest breath of neutralization activity despite comparable

252 binding antibody titers. This phenomenon was most noticeable at 14 DPC, and was still evident

253 28 DPC when the humoral response is more mature. Moreover, the overall neutralization

254 activity, regardless of initial challenge virus, against B.1.351 is much lower than the other two

255 variants, suggesting that B.1.351 may have indeed an enhanced ability to evade humoral

256 immune responses. The overall IgG response of the infected hamsters did not result in robust

257 differences amongst the variants; however, the neutralization cross-protection depended on

258 the variant the hamster was initially exposed to. Our data demonstrates that early in the

259 humoral response (14 DPC) antibodies induced by B.1.1.7 infection show an increased

260 crossrreacitvity compared to the other variants tested. By 28 DPC, when the humoral response

261 is more mature, this differences is less prominent, but the trend remains the same. This

262 observation suggests that the timing of the antibody response could affect the crossreactivity

263 potential. Notably, the neutralization capacity of crossreactive antibodies and homologous

264 antibodies against B.1.351 is much lower than that of the other two variants tested. This

265 observation is reflective of previous studies that attribute increased antibody evasion to this

266 VOC[3,4,8-10,12,21,22], demonstrating that the hamster model reflects the differences in humoral

267 responses and effectivity of prior immunity seen in clinical cases[29].

268 A significant challenge when using the hamster model is the lack of reagents to analyze cellular

269 immune responses[30-36]. Therefore, we employed transcriptomic analysis to elucidate

270 differences in the host responses to VOC compared to the ancestral variant in the lungs of

271 hamster 4 DPC, as has been done for other studies [37-39]. Our transcriptional analysis of lung

272 tissues at peak infection identified distinct, but also overlapping transcriptional signatures for

273 each variant. All infections exhibited gene expression patterns associated with innate antiviral

274   responses, notably type I IFN signaling, mobilization of lymphocytes, and apoptosis[40-43]. The

275   type I IFN response is critical for rapid control of viral infection[44]. However, dysregulated innate

276   immune and type I IFN responses can result in tissue damage and oxidative stress as noted in

277   other viral infections, including influenza virus and Ebola virus in addition to severe COVID-

278   19[40,41,45,46]. Our data differs from those reported in studies where a suppressed IFN response in

279   the peripheral blood, the bronchoalveolar lavage, and lungs obtained at autopsy from

280   individuals with severe COVID-19[47-52]. A potential explanation for this difference is the fact that

281   we profiled the lungs during the peak of viral replication and virus-induced pathology (4 DPC)

282   while clincal cases rarely present viral antigen at the time of death, rather immune

283   dysregulation and coagulation abnormalities are the casue of death[53-55]. Additionally, the Syrian

284   golden hamster model does not mimic severe COVID-19 intersitial pneumonia in that clinical

285   symptomology is less severe and none of the animals in this model succumb to disease.

286   Interestingly, transcriptional inflammatory indicators were particularly heightened following

287   infection with B.1.1.7 and least severe following infection with B.1.351. Expression of several

288   inflammatory and complement genes were only upregulated following infection with B.1.1.7

289   and ancestral variants, while *NFκB1* was upregulated only following infection with B.1.1.7[56,57].

290   *In vitro* and *in vivo* NFκB-driven inflammatory responses have been previously associated with

291   severe COVID-19[48,50,58,59]. Additionally, NK cell activation was evident by higher expression of

292   cytolytic molecules (e.g., *PRF1*). This inflammatory damage facilitates immune cell influx,

293   including inflammatory cells like neutrophils, which we predicted to increase in all infections[48].

294   Moreover, significant increases in IL-2-stimulated NK cells was also predicted following

295   infection with the ancestral and B.1.1.7 variants. Expression of canonical T cell regulatory and

296   exhaustion markers like *CTLA4*, *CD274* (PD-L1), and *FOXP3* suggests compensatory mechanisms

297   to reduce tissue damage.

298   Transcriptional changes were also predicted to result in significant B cell loss in the lungs

299   following infection with all three viruses. Previous studies indicate that B cell lymphopenia does

300   not preclude robust antibody responses[60-62]. This re-distribution could indicate B cell migration

301   to lymphoid tissue for priming. Indeed, significant neutralizing and binding antibody titers were

302   detected following all three infection, albeit lower following infection with B.1.135.

11

303   Furthermore, we detected a large number of DEGs related to tissue morphogenesis and

304   angiogenesis in all infections[63,64]. Microvascular injury can further exacerbate inflammation-

305   driven lung fibrosis[65]. Additionally, genes that play a role in tissue repair were downregulated

306   following infection with the B.1.351 and ancestral variants.

307   In this study we describe the pathogenesis of the SARS-CoV-2 variants and the development of

308   crossreactive neutralizing antibodies. To our knowledge this is the first study performing a

309   comparative and longitudinal analysis of the antibody response after SARS-CoV-2 VOC infection.

310   Our data show that infection with the B.1.1.7 VOC results in a broader antibody response

311   compared to infection with B.1.35 VOC. This broader response could be in part mediated by the

312   more robust transcriptional response elicited by this variant that includes a larger induction of

313   antiviral and inflammatory pathways. Future experiments should assess transcriptional changes

314   beyond 4 DPC to determine the kinetics of the host response at this critical site. Moreover,

315   additional studies should investigate the mechanisms by which the mutations detected in the

316   B.1.35 VOC lead to reduced neutralization potential.

317

318

319   **Methods**

320   *Ethics statement*

321   All infectious work with SARS-CoV-2 was performed in the containment laboratories at the

322   Rocky Mountain Laboratories (RML), Division of Intramural Research, National Institute of

323   Allergy and Infectious Diseases, National Institutes of Health. RML is an institution accredited by

324   the Association for Assessment and Accreditation of Laboratory Animal Care International

325   (AAALAC). All procedures followed standard operating procedures (SOPs) approved by the RML

326   Institutional Biosafety Committee (IBC)[66]. Animal work was performed in strict accordance with

327   the recommendations described in the Guide for the Care and Use of Laboratory Animals of the

328   National Institute of Health, the Office of Animal Welfare and the Animal Welfare Act, United

329   States Department of Agriculture. The studies were approved by the RML Animal Care and Use

330   Committee (ACUC). Procedures were conducted in animals anesthetized by trained personnel

331   under the supervision of veterinary staff. All efforts were made to ameliorate animal welfare

332   and minimize animal suffering; food and water were available *ad libitum*.

333

334   *Cells and Viruses*

335   VeroE6 cells were grown at 37°C and 5% CO_2 in Dulbecco's modified Eagle's medium (DMEM)

336   (Sigma-Aldrich, St. Louis, MO) containing 10% fetal bovine serum (FBS) (Wisent Inc., St. Bruno,

337   Canada), 2 mM L-glutamine (Thermo Fisher Scientific, Waltham, MA), 50 U/mL penicillin

338   (Thermo Fisher Scientific), and 50 µg/mL streptomycin (Thermo Fisher Scientific). SARS-CoV-2

339   ancestral isolate nCoV-WA1-2020 (MN985325.1)[67], SARS-CoV-2 isolate B.1.351 (hCoV-19/South

340   African/KRISP-K005325/2020), or SARS-CoV-2 isolate B.1.1.7

341   (hCOV_19/England/204820464/2020) were used for the neutralizing antibody assays. The

342   following reagent was obtained through BEI Resources, NIAID, NIH: Severe Acute Respiratory

343   Syndrome-Related Coronavirus 2, Isolate hCoV-19/England/204820464/20200, NR-54000,

344   contributed by Bassam Hallis. SARS-CoV-2 B. 1.351 was obtained with contributions from Dr.

345   Tulio de Oliveira and Dr. Alex Sigal (Nelson R Mandela School of Medicine, UKZN). All viruses

346   were grown and titered on Vero E6 cells, and sequence confirmed.

347

348   *Animal study*

349   Fifty female Syrian golden hamsters (5-8 weeks of age) were used in this study[14]. Five animals

350   were used as uninfected controls; three study cohorts for challenge with the ancestral virus and

351   variants B1.1.7 and B.1.351 consisted of 15 hamsters each. On day 0, hamsters were infected

352   with SARS-CoV-2 as previously described [14]. On 4, 14 and 28 DPC, 5 hamsters per group were

353   euthanized for sample collection.

354

355   *RNA extraction and RT-qPCR*

356   RNA from blood and oral swab samples was extracted using the QIAamp Viral RNA Mini Kit

357   (QIAGEN) according to manufacturer specifications. Lung tissue, a maximum of 30 mg each, was

358   processed and RNA was extracted using the RNeasy Mini Kit (QIAGEN) according to

359   manufacturer specifications. One step RT-qPCR for genomic viral RNA was performed using

360   specific primer-probe sets and the QuantiFast Probe RT-PCR +ROX Vial Kit (QIAGEN), in the

361   Rotor-Gene Q (QIAGEN) as described previously [68]. Five μL of each RNA extract were run

362   alongside dilutions of SARS-CoV-2 standards with a known concentration of RNA copies.

363

364   *Enzyme-linked immunosorbent assay*

365   Serum samples from SARS-CoV-2-infected animals were inactivated by gamma-irradiation and

366   used in BSL2 according to IBC-approved SOPs. NUNC Maxisorp Immuno plates were coated with

367   50 μl of 1 μg/mL of recombinant SARS-CoV-2 S (S1+S2) antigen at 4°C overnight and then

368   washed three times with PBS containing 0.05% Tween 20 (PBST). The plates were blocked with

369   3% skim milk in PBS for 1 hour at room temperature, followed by three additional washes with

370   PBST. The plates were incubated with 50 μl of serial dilutions of the samples in PBS containing

371   1% skim milk for 1 hour at room temperature. After three washes with PBST, the bound

372   antibodies were labeled using 50 μl of 1:2,500 peroxidase anti-hamster IgG (H+L) (SeraCare Life

373   Sciences) diluted in 1% skim milk in PBST. After incubation for 1 hour at room temperature and

374   three washes with PBST, 50 μl of KPL ABTS peroxidase substrate solution mix (SeraCare Life

375   Sciences) was added to each well, and the mixture was incubated for 30 min at room

376   temperature. The optical density (OD) at 405 nm was measured using a GloMax® explorer

377   (Promega). The OD values were normalized to the baseline samples obtained with naïve

378   hamster serum and the cutoff value was set as the mean OD plus standard deviation of the

379   blank.

380

381   *Virus neutralization assay*

382   The day before this assay, VeroE6 cells were seeded in 96-well plates. Serum samples were

383   heat-inactivated for 30 min at 56°C, and 2-fold serial dilutions were prepared in DMEM with 2%

384   FBS. Next, 100 $TCID_{50}$ of SARS-CoV-2 were added and the mixture was incubated for 1 hour at

385   37°C and 5% CO_2. Finally, media was removed from cells and the mixture was added to VeroE6

386   cells and incubated at 37°C and 5% CO_2 for 6 days. Then the cytopathic effect (CPE) was

387   documented, and the virus neutralization titer was expressed as the reciprocal value of the

388   highest dilution of the serum which inhibited virus replication (no CPE).

389

Histology and immunohistochemistry

Necropsies and tissue sampling were performed according to IBC-approved SOPs. Tissues were fixed in 10% neutral buffered formalin with two changes, for a minimum of 7 days. Tissues were placed in cassettes and processed with a Sakura VIP-6 Tissue Tek, on a 12-hour automated schedule, using a graded series of ethanol, xylene, and ParaPlast Extra. Embedded tissues are sectioned at 5 µm and dried overnight at 42°C prior to staining. Specific anti-CoV immunoreactivity was detected using Sino Biological Inc. SARS-CoV/SARS-CoV-2 nucleocapsid antibody (Sino Biological cat#40143-MM05) at a 1:1000 dilution. The secondary antibody was the Vector Laboratories ImPress VR anti-mouse IgG polymer (cat# MP-7422). The tissues were then processed for immunohistochemistry using the Discovery Ultra automated stainer (Ventana Medical Systems) with a ChromoMap DAB kit (Roche Tissue Diagnostics cat#760– 159). All tissue slides were evaluated by a board-certified veterinary pathologist and a pathology scored was assigned based on the following observations; 0= no pathology, 1= minimal, 2= mild, 3= moderate, 4= severe (Fig. S1C).

cDNA library construction and sequencing

Quality and quantity of RNA lung samples at 4 DPC were determined using an Agilent 2100 Bioanalyzer. cDNA libraries were constructed using the NEB Next Ultra II Direction RNA Library Prep Kit (Thermo Fischer). RNA was treated with RNase H and DNase I following depletion of ribosomal RNA (rRNA). Adapters were ligated to cDNA products and the subsequent ~300 base pair (bp) amplicons were PCR-amplified and selected by size exclusion. cDNA libraries were assessed for quality and quantity prior to 150 bp single-end sequencing using the Illumina NovaSeq platform.

RNA-Seq Bioinformatic analysis

Preliminary data analysis was performed with RNA-Seq workflow module of systemPipeR, developed by Backman *et. al* [69]. RNA-Seq reads were demultiplexed, quality-filtered and trimmed using Trim Galore (average Phred score cut-off of 30, minimum length of 50 bp).

418   FastQC was used to generate quality reports. Hisat2 was used to align reads to the reference

419   genome *Mesocricetus auratus* (Mesocricetus_auratus.MesAur1.0.dna.toplevel.fa) and the

420   Mesocricetus_auratus.MesAur1.0.103.gtf file was used for annotation. Raw expression values

421   (gene-level read counts) were generated using the summarizeOverlaps function and normalized

422   (read per kilobase of transcript per million mapped reads, rpkm) using the edgeR package.

423   Statistical analysis with edgeR was used to determine differentially expressed genes (DEGs)

424   meeting the following criteria: genes with median rpkm of ≥1, a false discovery rate (FDR)

425   corrected p-value ≤ 0.05 and a $\log_2$fold change ≥ 1 compared to control tissues.

426   Functional enrichment of DEGs was performed using Metascape to identify relevant GO

427   terms[70]. Digital cell quantification was performed using ImmQuant with the IRIS database.

428   Heatmaps, bubbleplots, Venn diagrams and violin plots were generated using R packages

429   ggplot2 and VennDiagrams. Graphs were generated using GraphPad Prism software (version 8).

430

431   *SARS-CoV-2 viral genome library construction and sequencing*

432   Enrichment of SARS-CoV-2 was performed using the Qiagen QIASeq SARS-CoV-2 Primer Panel

433   (V.2). Libraries were constructed from resulting SARS-CoV-2 amplicons using the Qiagen QIASeq

434   FX DNA Library preparation kit. Briefly, adapters were ligated to cDNA products and the ~300

435   bp amplicons were minimally PCR-amplified. cDNA libraries were assessed for quality and

436   quantity prior to 150 bp paired-end sequencing using the Illumina HiSeq platform (≥ 1 M reads

437   per sample).

438

439   *SARS-CoV-2 viral genome assembly and bioinformatic analysis*

440   Reads were demultiplexed and quality-filtered using Trim Galore (average Phred score cut-off

441   of 30, minimum length 100 bp). FastQC was used to generate quality reports. MaskPrimers.py

442   from the pRESTO R package was used to remove primers prior to alignment to the SARS-CoV-2

443   genome using BWA-mem software version 0.7.17. The following reference genomes were used

444   for Ancestral, B.1.1.7 and B.1.351 variants: WA_MN985325.1, EPI_ISL_683466, and

445   EPI_ISL_6786156. All genomes had greater than 95% coverage and 10X depth. Single nucleotide

446   polymorphisms and amino acid changes were identified using CorGAT.

447

448   *Statistical analyses*

449   All statistical analysis was performed in Prism 8 (GraphPad). Two-tailed Mann-Whitney test was

450   conducted to compare differences between groups for data in Figs. 2, 3 and S1. Statistical

451   significance was determined using one-way ANOVA with multiple comparisons for the

452   bioinformatic analysis with comparisons made among variant- and control-challenged animals

453   Statistically significant differences are indicated as follows: $p < 0.0001$ (****), $p < 0.001$ (***),

454    $p < 0.01$ (**) and $p < 0.05$ (*).

455

456

457   **Data Availability**

458   All transcriptomic sequencing data are accessible at BioProject PRJNAXXXX upon publication.

459

460   **Acknowledgments**

461   We thank members of the Molecular Pathogenesis Unit, Virus Ecology Section, and Research

462   Technology Branch (all NIAID) for their efforts to obtain and characterize the SARS-CoV-2

463   isolates. We also thank the Rocky Mountain Veterinary Branch, NIAID for supporting the animal

464   studies, and Anita Mora (NIAID) for assistance generating the pathology figures.

465

466

467   **Author contributions**

468   A.M. conceived the idea and secured funding. K.L.O., I.M, and A.M. designed the studies. K.L.O.,

469   C.S.C., K.S., T.G., P.F., and A.M. conducted the animal studies, processed the samples and

470   acquired the data. A.N.P. performed transcriptomics analysis and viral genome sequencing.

471   K.L.O., A.N.P., C.S.C., I.M., and A.M. analyzed and interpreted the data. K.L.O., A.N.P., I.M., and

472   A.M. prepared the manuscript with input from all authors. All authors approved the

473   manuscript.

474

475   **Funding**

476   The study was funded by the Intramural Research Program, NIAID, NIH and in part by the

477   National Center for Research Resources and the National Center for Advancing Translational

478   Sciences, NIH, through grants UL1TR001414-06 and 1R01AI152258-01 awarded to I.M.

479

480   **Competing interest**
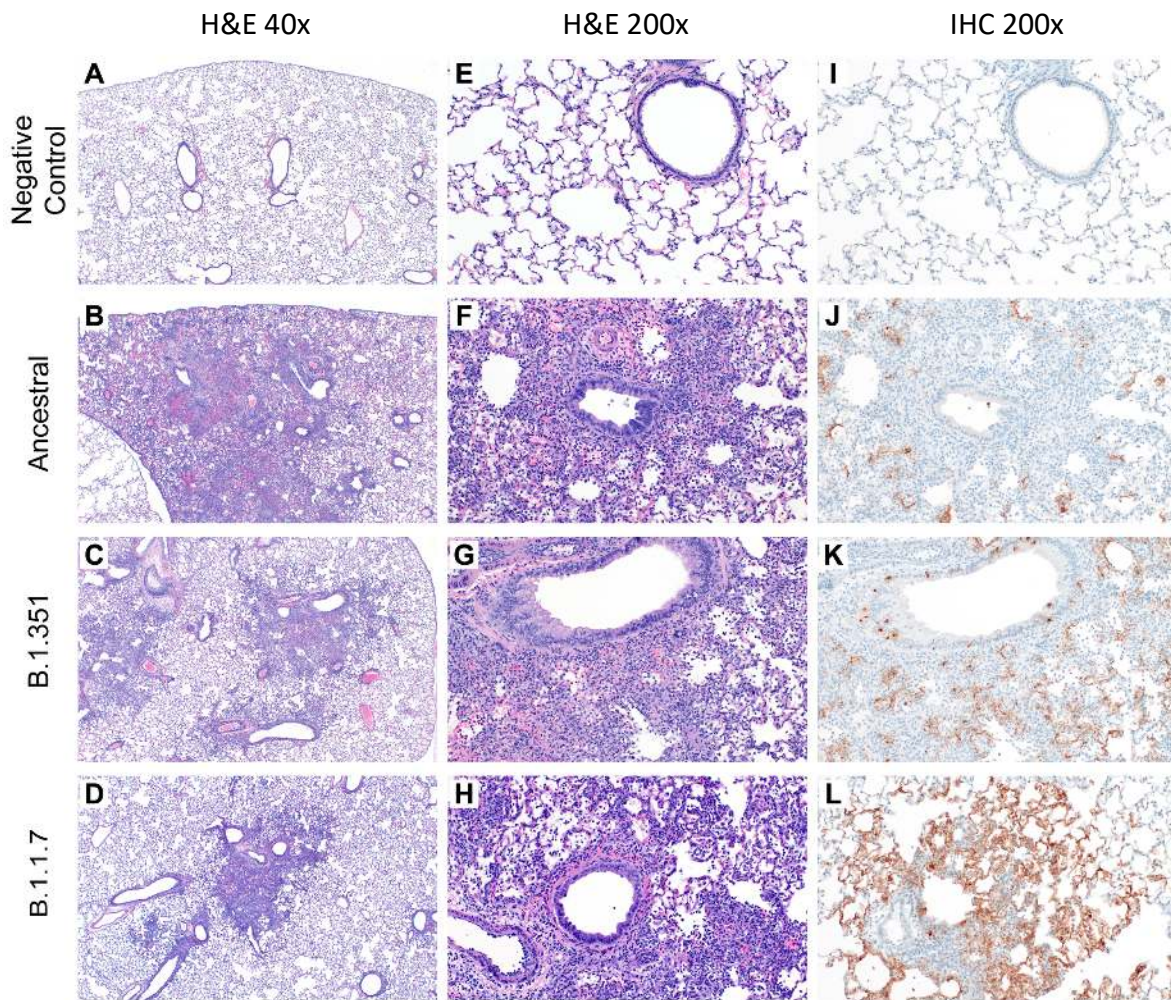
481   The authors declare no conflicts of interest.

482

483

484

485

**Fig. 1. Histopathology and Immunohistochemistry of hamster lungs. (A-H)** Representative H&E images of lungs of hamsters infected with 10^5 TCID$_{50}$ of ancestral, B.1.1.7, and B.1.351 variants at 4 days post-challenge (DPC). Foci of interstitial pneumonia and bronchiolitis were observed throughout all evaluated lung lobes of infected hamsters. **(I-L)** Immunohistochemistry (IHC) detected SARS-CoV-2 nucleocapsid staining in the lungs of all infected hamsters.
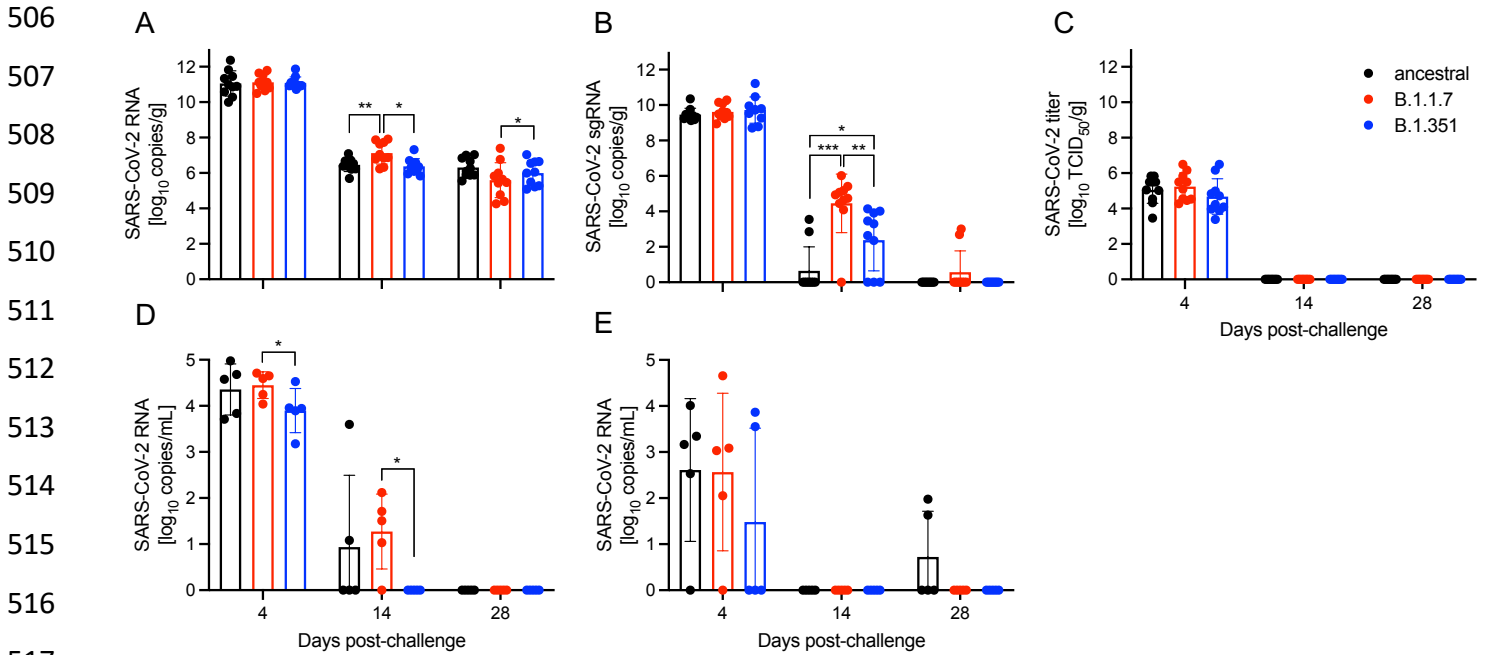
Fig. 2. SARS-CoV-2 burden in lungs, oral swabs and blood. (A) Total SARS-CoV-2-specific RNA and **(B)** total SARS-CoV-2-specific sub-genomic RNA (sgRNA) in the lungs of challenged animals at 4, 14, and 28 days post-challenge (DPC). **(C)** Infectious SARS-CoV-2 titer in the lungs of infected hamsters. Total SARS-CoV-2-specific RNA in the **(D)** oral swabs and **(E)** blood of infected hamsters at the time of euthanasia. Geometric mean and standard deviation (SD) are depicted; statistical significance is indicated ***p < 0.001, **p < 0.01 and *p < 0.05.
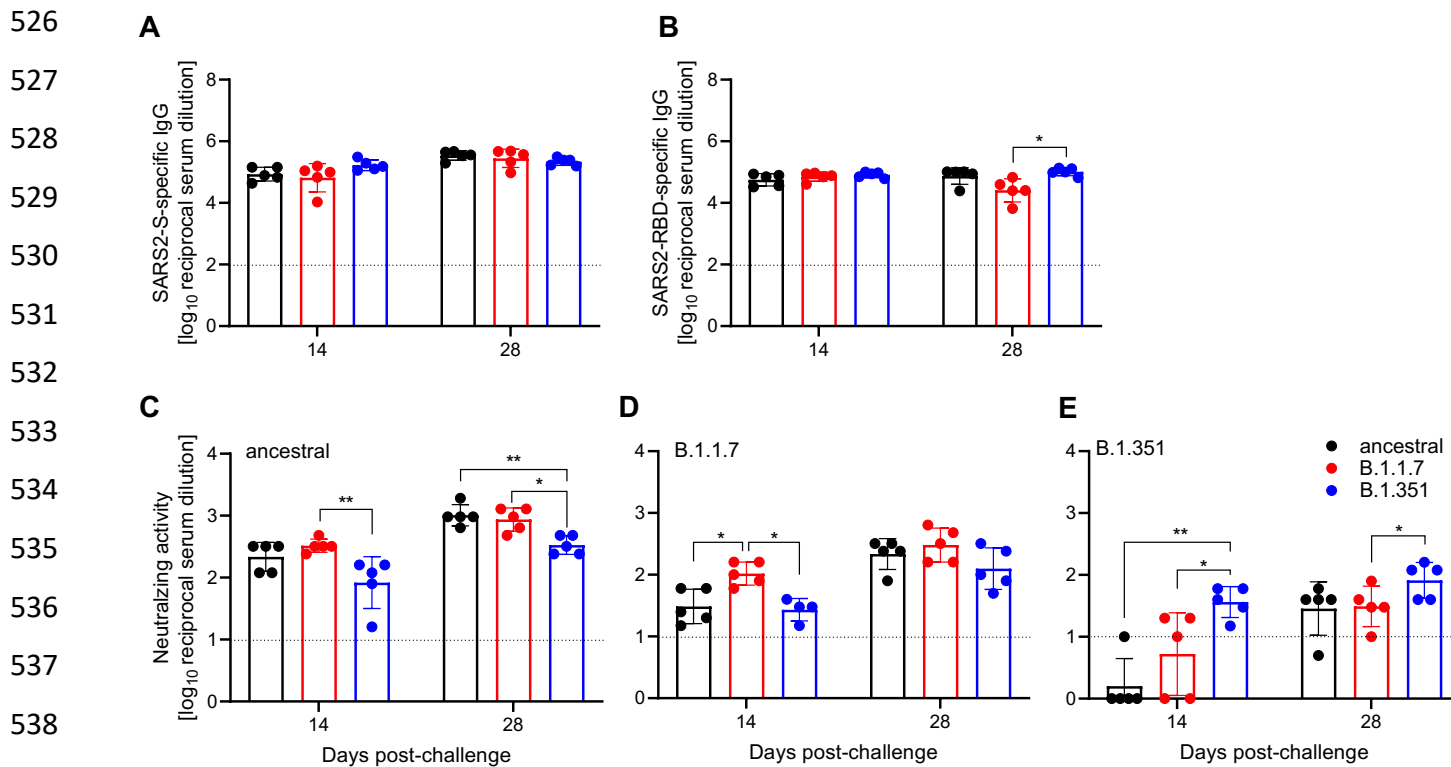
Fig. 3. Humoral immune response in challenged hamsters. Serum samples were collected at 14 and 28 DPC and by ELISA. **(A)** Total SARS-CoV-2 S-specific IgG and **(B)** RBD-specific IgG are shown. Cross-variant and homologous neutralization was assessed against **(C)** ancestral, **(D)** B.1.1.7, and (E) B.1.351 viruses. Line indicates limit of detection. Geometric mean and SD are depicted; statistical significance is indicated $**p < 0.01$ and $*p < 0.05$.

547

548

549

550

551

552

553

554

555

556

557

558

559

560

561

562

563

564

565

566

567

568

569

570

571

572

573

574

575

22
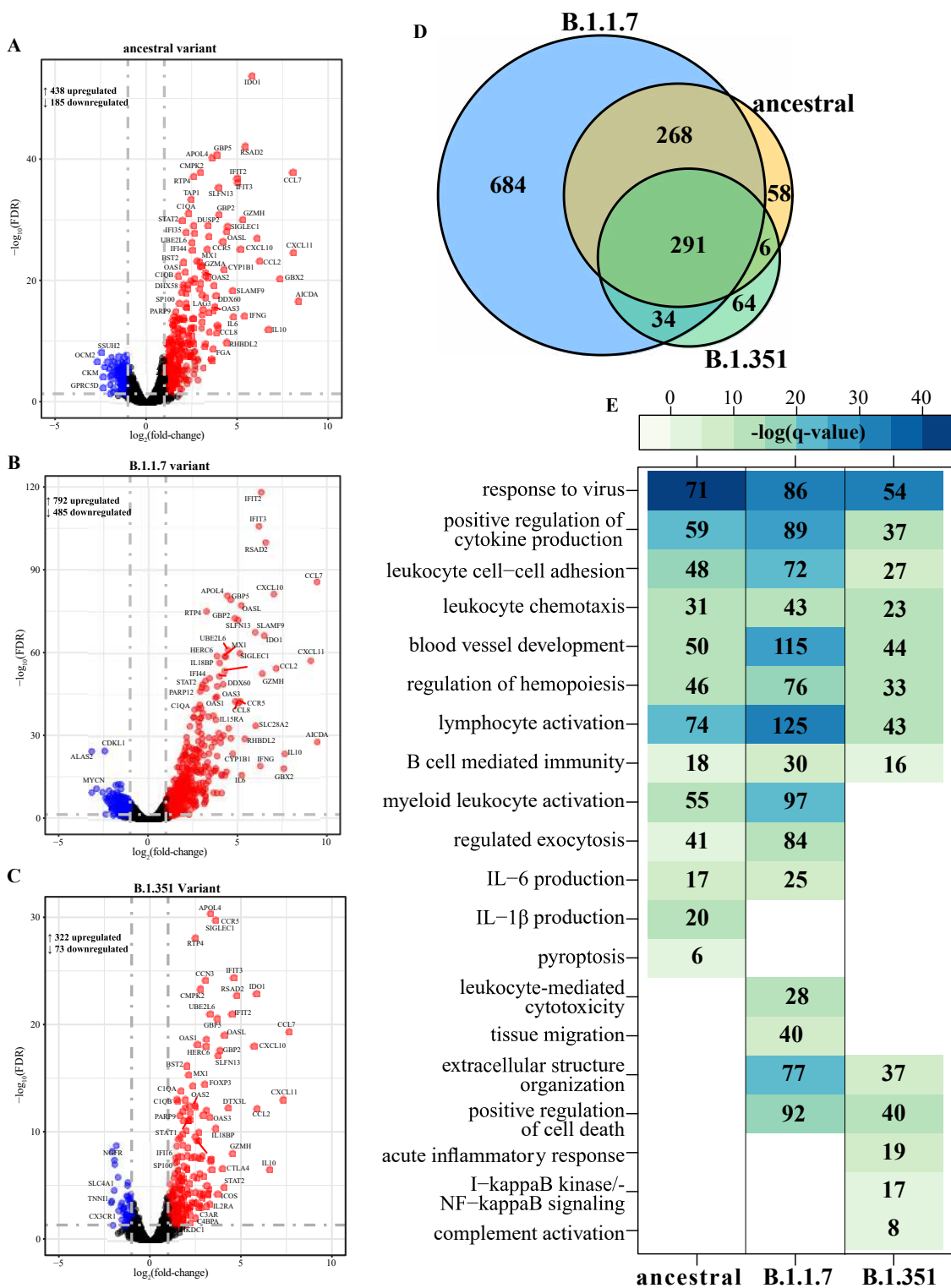
576

577 **Fig. 4. SARS-CoV-2 variants induce distinct transcriptional changes.** Volcano plot of global gene

578 expression changes at 4 DPC with SARS-CoV-2 **(A)** ancestral, **(B)** B.1.1.7 or **(C)** B.1.351 variants.

579 Downregulated and upregulated differentially expressed genes (DEGs; average RPKM $\geq$ 1) are

580 colored blue and red, respectively. Exemplary genes are labeled. **(D)** Venn diagram of DEGs

581 determined in panels A-C. **(E)** Functional enrichment of DEGs determined following each

582 infection in panels A-C. Color intensity represents statistical significance as the negative log of

583 the FDR-adjusted p-value [-log(q-value)], with range of colors based on the GO terms with the

584 lowest and highest statistical value for all GO terms present. Blank boxes indicate no statistical

585 significance. Numbers of DEGs enriching to each GO term are noted in each box.

586

587

588

589

590

591

592

593

594

595

596

597

598

599

600

601

602

603

604

605

606

607

608

609

610

611

612

613

614

615

24
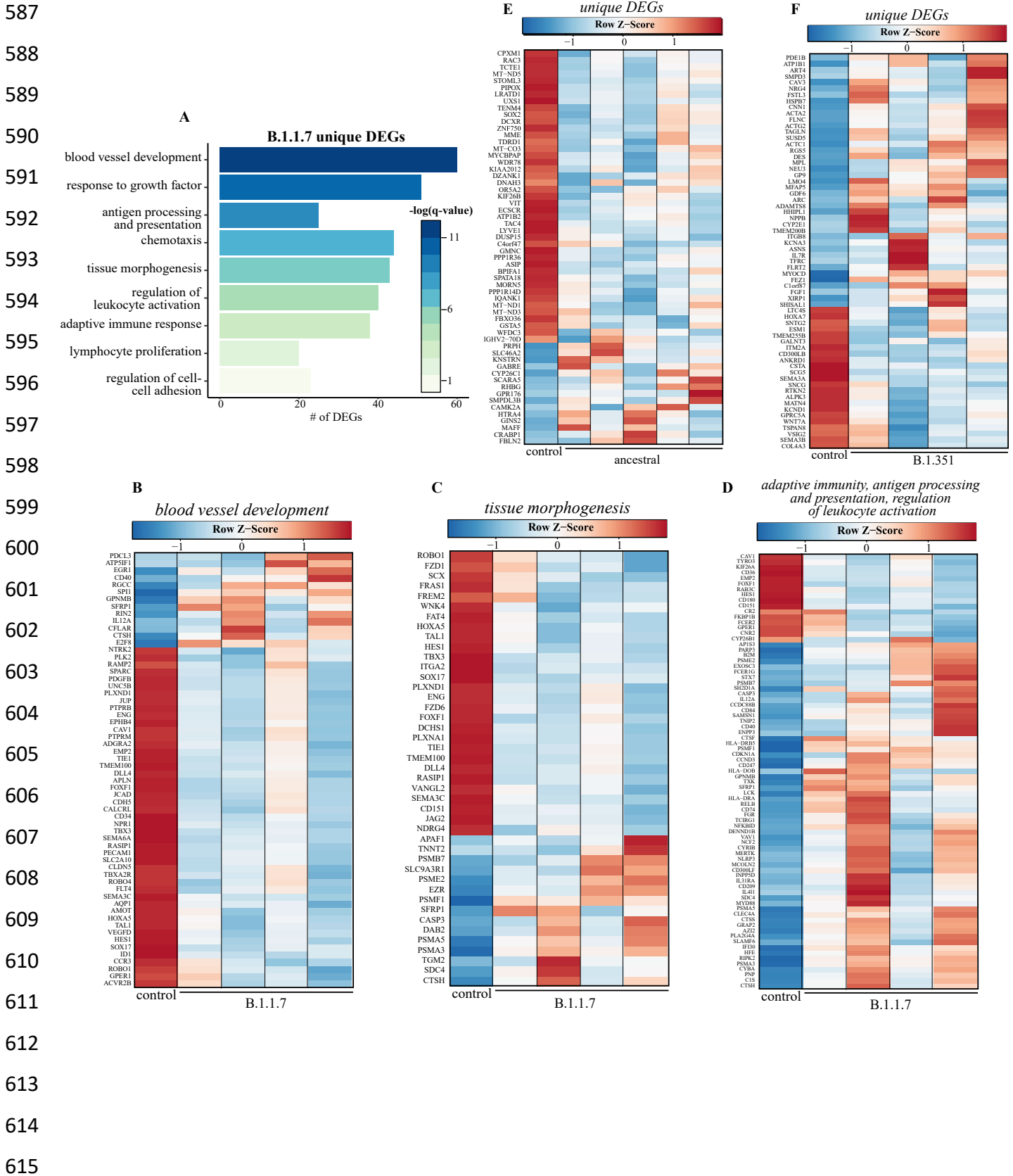
616 **Fig. 5. Transcriptional response unique to B.1.1.7 variant suggests distinct host responses.**

617 **(A)** Functional enrichment of DEGs unique to B.1.1.7 variant infection at 4 DPC (n=684).

618 Horizontal bars represent the number of genes enriching to each GO term with color intensity

619 representing the negative log of the FDR-adjusted p-value [-log(q-value)]. Range of colors based

620 on the GO terms with the lowest and highest –log(q-value) values. Heatmaps representing

621 B.1.1.7 variant unique DEGs enriching to GO terms from panel A: **(B)** "blood vessel

622 development", **(C)** "tissue morphogenesis" and **(D)** adaptive terms "adaptive immunity",

623 "antigen processing and presentation", and "regulation of leukocyte activation." Heatmaps of

624 DEGs unique to **(E)** Ancestral (n=58) and **(F)** B.1.351 variants (n=64) at 4 DPC. Columns of all

625 heatmaps represent the average rpkm of controls and rpkm of a single variant-infected animal.

626 Range of colors per each heatmap is based on scaled and centered rpkm values of the

627 represented DEGs. Red represents upregulation; blue, downregulation.

628

629

630 **Table 1. Genome comparison of SARS-CoV-2 variants**

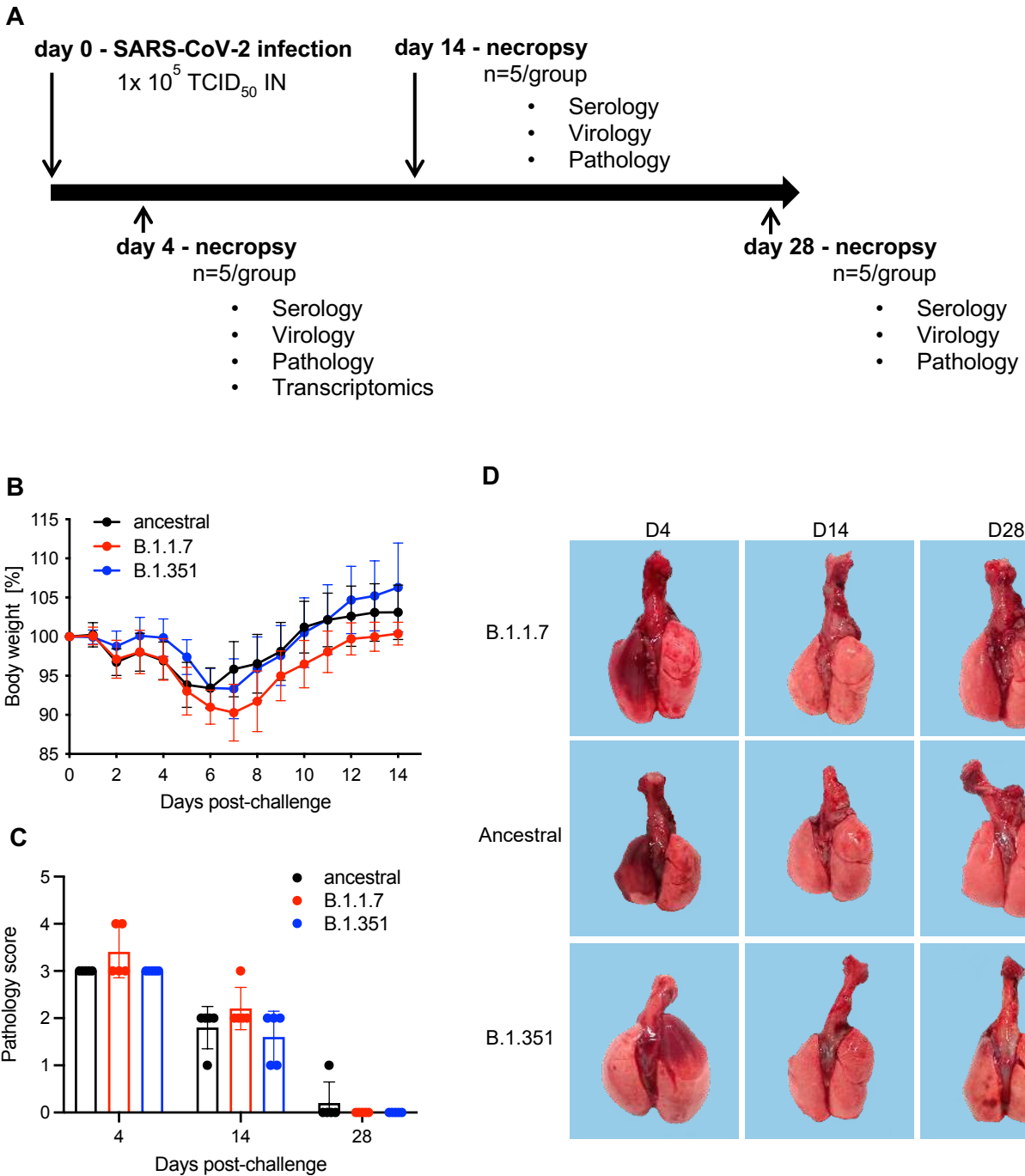| Variant of concern	Amino acid changes (# of animals affected, 4 DPC)
ancestral	none detected
B.1.1.7	none detected
B.1.351	5' UTR, T201C (5/5) nsp3, L3892F (1/5) nsp3, G5942G (5/5) ORF3a, G172C (5/5)

631

632

633

25

634

Figure S1. Study outline, body weight changes and pathology of infected hamsters. (A) Schematic study outline. (B) Body weight changes in hamsters (n=10/group). (C) Evidence of interstitial pneumonia was recorded in histopathology samples. (D) Representative pictures of hamster lungs with lesions during disease progression. Gross lung images at day (D) 4 , 14 and 28 post-challenge.
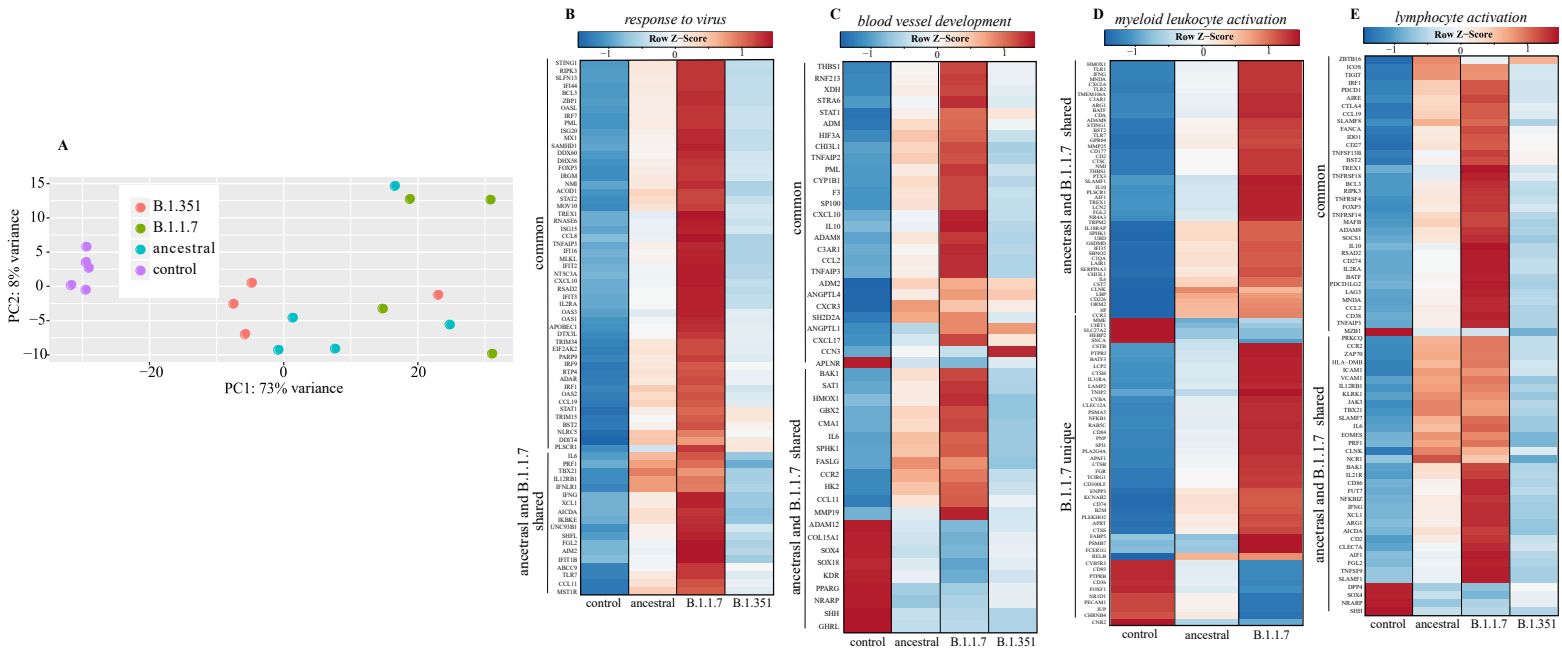
635

Figure S2. SARS-CoV-2 variants induce distinct transcriptional changes. (A) Principal component analysis of control (n=5) animals and infected animals 4 DPC with ancestral (n=5), B.1.1.7 (n=4) or B.1.351 (n=4) variants. Heatmaps representing DEGs enriching to GO terms from Fig. 5E including (B) "response to virus", (C) "blood vessel development", (D) "myeloid leukocyte activation" and (E) lymphocyte activation." DEGs are either shared among all variant infections or between ancestral and B.1.1.7 variant infections. Columns of all heatmaps represent the average rpkm. Range of colors per each heatmap is based on scaled and centered rpkm values of the represented DEGs. Red represents upregulation; blue, downregulation.
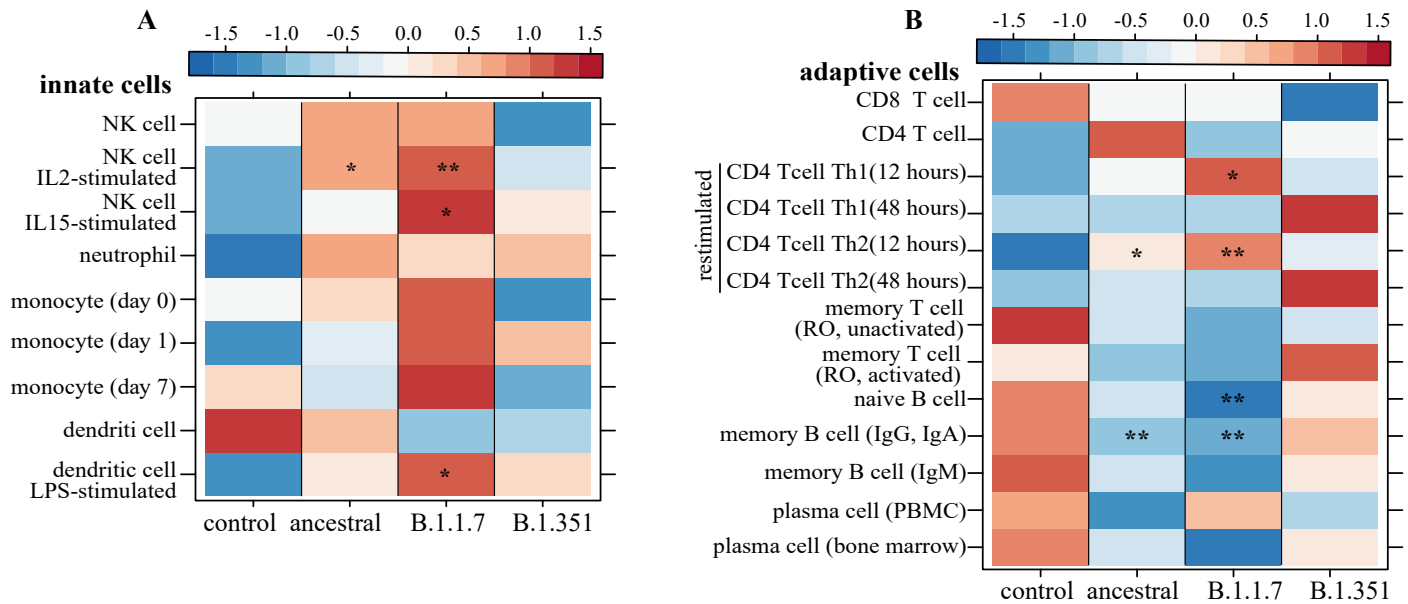
636

Figure S3. Digital cell quantification in hamster lungs. Heatmaps representing relative changes in (A) innate and (B) adaptive immune cell frequencies using ImmQuant with IRIS database. Each column represents the average relative expression level of the given immune cell. Range of colors per each heatmap is based on scaled and centered relative expression values. Red represents upregulation; blue represents downregulation. Statistical significance is indicated **p < 0.01 and *p < 0.05.

References

1   Song, F. *et al.* Emerging 2019 Novel Coronavirus (2019-nCoV) Pneumonia. *Radiology* **295**, 210-217, doi:10.1148/radiol.2020200274 (2020).

2   Prevention, C. f. D. C. a. *Science Brief: emerging SARS-CoV-2 variants*, <https://www.cdc.gov/ coronavirus/2019-ncov/more/science-and-research/scientif ic-brief -emerging-variants.html> (2021).

3   Leung, K., Shum, M. H., Leung, G. M., Lam, T. T. & Wu, J. T. Early transmissibility assessment of the N501Y mutant strains of SARS-CoV-2 in the United Kingdom, October to November 2020. *Euro Surveill* **26**, doi:10.2807/1560-7917.ES.2020.26.1.2002106 (2021).

4   Luan, B., Wang, H. & Huynh, T. Enhanced binding of the N501Y-mutated SARS-CoV-2 spike protein to the human ACE2 receptor: insights from molecular dynamics simulations. *FEBS Lett* **595**, 1454-1461, doi:10.1002/1873-3468.14076 (2021).

5   Youngfei Cai, J. Z., Tianshu Xiao, Christy L. Lavine, et al. Structural basis for enhanced infectivity and immune evasion of SARS-CoV-2 variants. *Science*, doi:10.1126/science.abi9745 (2021).

6   Andrew Rambaut, N. L., Oliver Pybus, Wendy Barclay, Jeff Barrett, Alesandro Carabelli6 Tom Connor, Tom Peacock, David L Robertson, Erik Volz. *Preliminary genomic characterisation of an emergent SARS-CoV-2 lineage in the UK defined by a novel set of spike mutations*, <https://virological.org/t/preliminary-genomic-characterisation-of-an-emergent-sars-cov-2-lineage-in-the-uk-defined-by-a-novel-set-of-spike-mutations/563> (2020).

7   Nuno R. Faria, I. M. C., Darlan Candido. Genomic characterisation of an emergent SARS-CoV-2 lineage in Manaus Genomic *Virological* (2021).

8   Chen, R. E. *et al.* Resistance of SARS-CoV-2 variants to neutralization by monoclonal and serum-derived polyclonal antibodies. *Nat Med* **27**, 717-726, doi:10.1038/s41591-021-01294-w (2021).

9   Liu, Y. *et al.* Neutralizing Activity of BNT162b2-Elicited Serum. *N Engl J Med* **384**, 1466-1468, doi:10.1056/NEJMc2102017 (2021).

10   Wibmer, C. K. *et al.* SARS-CoV-2 501Y.V2 escapes neutralization by South African COVID-19 donor plasma. *Nat Med* **27**, 622-625, doi:10.1038/s41591-021-01285-x (2021).

11   Wang, C., Horby, P. W., Hayden, F. G. & Gao, G. F. A novel coronavirus outbreak of global health concern. *The Lancet* **395**, 470-473, doi:10.1016/s0140-6736(20)30185-9 (2020).

12   Nuno R. Faria, I. M. C., Darlan Candido. Genomic characterisation of an emergent SARS-CoV-2 lineage in Manaus: preliminary findings. *Virological* (2021).

13   Deng, X. *et al.* Transmission, infectivity, and neutralization of a spike L452R SARS-CoV-2 variant. *Cell* **184**, 3426-3437 e3428, doi:10.1016/j.cell.2021.04.025 (2021).

14   Rosenke, K. *et al.* Defining the Syrian hamster as a highly susceptible preclinical model for SARS-CoV-2 infection. *Emerg Microbes Infect* **9**, 2673-2684, doi:10.1080/22221751.2020.1858177 (2020).

15   Sia, S. F. *et al.* Pathogenesis and transmission of SARS-CoV-2 in golden hamsters. *Nature* **583**, 834-838, doi:10.1038/s41586-020-2342-5 (2020).

16   Sola, I., Almazan, F., Zuniga, S. & Enjuanes, L. Continuous and Discontinuous RNA Synthesis in Coronaviruses. *Annu Rev Virol* **2**, 265-288, doi:10.1146/annurev-virology-100114-055218 (2015).

17   Sawicki, S. G., Sawicki, D. L. & Siddell, S. G. A contemporary view of coronavirus transcription. *J Virol* **81**, 20-29, doi:10.1128/JVI.01358-06 (2007).

18   Abbas, A. R. *et al.* Immune response in silico (IRIS): immune-specific genes identified from a compendium of microarray expression data. *Genes Immun* **6**, 319-331, doi:10.1038/sj.gene.6364173 (2005).

19   Davies, N. G. *et al.* Estimated transmissibility and impact of SARS-CoV-2 lineage B.1.1.7 in England. *Science* **372**, doi:10.1126/science.abg3055 (2021).

20   Li, Q. *et al.* Early Transmission Dynamics in Wuhan, China, of Novel Coronavirus-Infected Pneumonia. *N Engl J Med* **382**, 1199-1207, doi:10.1056/NEJMoa2001316 (2020).

21   Greaney, A. J. *et al.* Complete Mapping of Mutations to the SARS-CoV-2 Spike Receptor-Binding Domain that Escape Antibody Recognition. *Cell Host Microbe* **29**, 44-57 e49, doi:10.1016/j.chom.2020.11.007 (2021).

22   Wang, Z. *et al.* mRNA vaccine-elicited antibodies to SARS-CoV-2 and circulating variants. *Nature* **592**, 616-622, doi:10.1038/s41586-021-03324-6 (2021).

23 Abdelnabi, R. *et al.* Comparing infectivity and virulence of emerging SARS-CoV-2 variants in Syrian hamsters. *EBioMedicine* **68**, 103403, doi:10.1016/j.ebiom.2021.103403 (2021).

24 Imai, M. *et al.* Syrian hamsters as a small animal model for SARS-CoV-2 infection and countermeasure development. *Proc Natl Acad Sci U S A* **117**, 16587-16595, doi:10.1073/pnas.2009799117 (2020).

25 Chan, J. F. *et al.* Simulation of the Clinical and Pathological Manifestations of Coronavirus Disease 2019 (COVID-19) in a Golden Syrian Hamster Model: Implications for Disease Pathogenesis and Transmissibility. *Clin Infect Dis* **71**, 2428-2446, doi:10.1093/cid/ciaa325 (2020).

26 Abdelnabi, R. *et al.*, doi:10.1101/2021.02.26.433062 (2021).

27 Lei, X. *et al.* Activation and evasion of type I interferon responses by SARS-CoV-2. *Nat Commun* **11**, 3810, doi:10.1038/s41467-020-17665-9 (2020).

28 Xia, H. *et al.* Evasion of Type I Interferon by SARS-CoV-2. *Cell Rep* **33**, 108234, doi:10.1016/j.celrep.2020.108234 (2020).

29 Sabino, E. C. *et al.* Resurgence of COVID-19 in Manaus, Brazil, despite high seroprevalence. *The Lancet* **397**, 452-455, doi:10.1016/s0140-6736(21)00183-5 (2021).

30 Ebihara, H. *et al.* A Syrian golden hamster model recapitulating ebola hemorrhagic fever. *J Infect Dis* **207**, 306-318, doi:10.1093/infdis/jis626 (2013).

31 DeBuysscher, B. L. *et al.* Comparison of the pathogenicity of Nipah virus isolates from Bangladesh and Malaysia in the Syrian hamster. *PLoS Negl Trop Dis* **7**, e2024, doi:10.1371/journal.pntd.0002024 (2013).

32 Hammerbeck, C. D. & Hooper, J. W. T cells are not required for pathogenesis in the Syrian hamster model of hantavirus pulmonary syndrome. *J Virol* **85**, 9929-9944, doi:10.1128/JVI.05356-11 (2011).

33 Prescott, J. *et al.* The adaptive immune response does not influence hantavirus disease or persistence in the Syrian hamster. *Immunology* **140**, 168-178, doi:10.1111/imm.12116 (2013).

34 Safronetz, D. *et al.* Adenovirus vectors expressing hantavirus proteins protect hamsters against lethal challenge with andes virus. *J Virol* **83**, 7285-7295, doi:10.1128/JVI.00373-09 (2009).

35 Safronetz, D. *et al.* Hamster-adapted Sin Nombre virus causes disseminated infection and efficiently replicates in pulmonary endothelial cells without signs of disease. *J Virol* **87**, 4778-4782, doi:10.1128/JVI.03291-12 (2013).

36 Zivcec, M., Safronetz, D., Haddock, E., Feldmann, H. & Ebihara, H. Validation of assays to monitor immune responses in the Syrian golden hamster (Mesocricetus auratus). *J Immunol Methods* **368**, 24-35, doi:10.1016/j.jim.2011.02.004 (2011).

37 Falcinelli, S. *et al.* Characterization of the host response to pichinde virus infection in the Syrian golden hamster by species-specific kinome analysis. *Mol Cell Proteomics* **14**, 646-657, doi:10.1074/mcp.M114.045443 (2015).

38 Tchitchek N, S. D., Rasmussen AL. Sequencing, annotation and analysis of the Syrian hamster (Mesocricetus auratus) transcriptome. *Plos one* **9**, doi:10.6070/H4FQ9TKP (2014).

39 Ying, B., Toth, K., Spencer, J. F., Aurora, R. & Wold, W. S. Transcriptome sequencing and development of an expression microarray platform for liver infection in adenovirus type 5-infected Syrian golden hamsters. *Virology* **485**, 305-312, doi:10.1016/j.virol.2015.07.024 (2015).

40 Mortaz, E., Tabarsi, P., Varahram, M., Folkerts, G. & Adcock, I. M. The Immune Response and Immunopathology of COVID-19. *Frontiers in Immunology* **11**, doi:10.3389/fimmu.2020.02037 (2020).

41 Schurink, B. *et al.* Viral presence and immunopathology in patients with lethal COVID-19: a prospective autopsy cohort study. *The Lancet Microbe* **1**, e290-e299, doi:10.1016/S2666-5247(20)30144-0 (2020).

42 Tahaghoghi-Hajghorbani, S. *et al.* The role of dysregulated immune responses in COVID-19 pathogenesis. *Virus Research* **290**, 198197, doi:10.1016/j.virusres.2020.198197 (2020).

43 Wang, D. *et al.* Clinical Characteristics of 138 Hospitalized Patients With 2019 Novel Coronavirus–Infected Pneumonia in Wuhan, China. *JAMA* **323**, 1061-1069, doi:10.1001/jama.2020.1585 (2020).

44 Randall, R. E. & Goodbourn, S. Interferons and viruses: an interplay between induction, signalling, antiviral responses and virus countermeasures. *J Gen Virol* **89**, 1-47, doi:10.1099/vir.0.83391-0 (2008).

45 Davidson, S., Crotta, S., McCabe, T. M. & Wack, A. Pathogenic potential of interferon alphabeta in acute influenza infection. *Nat Commun* **5**, 3864, doi:10.1038/ncomms4864 (2014).

46 Liu, X. *et al.* Transcriptomic signatures differentiate survival from fatal outcomes in humans infected with Ebola virus. *Genome Biol* **18**, 4, doi:10.1186/s13059-016-1137-3 (2017).

740 47 Bost, P. *et al.* Host-Viral Infection Maps Reveal Signatures of Severe COVID-19 Patients. *Cell* **181**, 1475-
741   1488.e1412, doi:10.1016/j.cell.2020.05.006 (2020).
742 48 Hadjadj, J. *et al.* Impaired type I interferon activity and inflammatory responses in severe COVID-19
743   patients. *Science* **369**, 718-724, doi:10.1126/science.abc6027 (2020).
744 49 Islam, A. B. M. M. K. & Khan, M. A.-A.-K. Lung transcriptome of a COVID-19 patient and systems biology
745   predictions suggest impaired surfactant production which may be druggable by surfactant therapy.
746   *Scientific Reports* **10**, 19395, doi:10.1038/s41598-020-76404-8 (2020).
747 50 Major, J. *et al.* Type I and III interferons disrupt lung epithelial repair during recovery from viral infection.
748   *Science* **369**, 712-717, doi:10.1126/science.abc2061 (2020).
749 51 Speranza, E. *et al.* Single-cell RNA sequencing reveals SARS-CoV-2 infection dynamics in lungs of African
750   green monkeys. *Science Translational Medicine* **13**, doi:10.1126/scitranslmed.abe8146 (2021).
751 52 Wu, M. *et al.* Transcriptional and proteomic insights into the host response in fatal COVID-19 cases.
752   *Proceedings of the National Academy of Sciences* **117**, 28336-28343, doi:10.1073/pnas.2018030117
753   (2020).
754 53 Huang, C. *et al.* Clinical features of patients infected with 2019 novel coronavirus in Wuhan, China. *The*
755   *Lancet* **395**, 497-506, doi:10.1016/s0140-6736(20)30183-5 (2020).
756 54 Chen, T. *et al.* Clinical characteristics of 113 deceased patients with coronavirus disease 2019:
757   retrospective study. *BMJ* **368**, m1091, doi:10.1136/bmj.m1091 (2020).
758 55 Wu Z, M. J. haracteristics of and Important Lessons From the Coronavirus Disease 2019 (COVID-19)
759   Outbreak in China: Summary of a Report of 72 314 Cases From the Chinese Center for Disease Control and
760   Prevention. . *JAMA* **323**, 1239-1242, doi:10.1001/jama.2020.2648 (2020).
761 56 Chen, G. *et al.* Clinical and immunological features of severe and moderate coronavirus disease 2019. *J*
762   *Clin Invest* **130**, 2620-2629, doi:10.1172/JCI137244 (2020).
763 57 Herold, T. *et al.* Elevated levels of IL-6 and CRP predict the need for mechanical ventilation in COVID-19. *J*
764   *Allergy Clin Immunol* **146**, 128-136 e124, doi:10.1016/j.jaci.2020.05.008 (2020).
765 58 Hariharan, A., Hakeem, A. R., Radhakrishnan, S., Reddy, M. S. & Rela, M. The Role and Therapeutic
766   Potential of NF-kappa-B Pathway in Severe COVID-19 Patients. *Inflammopharmacology*, 1-10,
767   doi:10.1007/s10787-020-00773-9 (2020).
768 59 Huang, J. *et al.* SARS-CoV-2 Infection of Pluripotent Stem Cell-Derived Human Lung Alveolar Type 2 Cells
769   Elicits a Rapid Epithelial-Intrinsic Inflammatory Response. *Cell Stem Cell* **27**, 962-973.e967,
770   doi:10.1016/j.stem.2020.09.013 (2020).
771 60 Garcia-Beltran, W. F. *et al.* COVID-19-neutralizing antibodies predict disease severity and survival. *Cell*
772   **184**, 476-488.e411, doi:10.1016/j.cell.2020.12.015 (2021).
773 61 Legros, V. *et al.* A longitudinal study of SARS-CoV-2-infected patients reveals a high correlation between
774   neutralizing antibodies and COVID-19 severity. *Cellular & Molecular Immunology* **18**, 318-327,
775   doi:10.1038/s41423-020-00588-2 (2021).
776 62 Röltgen, K. *et al.* Defining the features and duration of antibody responses to SARS-CoV-2 infection
777   associated with disease severity and outcome. *Science Immunology* **5**, doi:10.1126/sciimmunol.abe0240
778   (2020).
779 63 Bradley, B. T. *et al.* Histopathology and ultrastructural findings of fatal COVID-19 infections in Washington
780   State: a case series. *The Lancet* **396**, 320-332, doi:10.1016/S0140-6736(20)31305-2 (2020).
781 64 Martines, R. B. *et al.* Pathology and Pathogenesis of SARS-CoV-2 Associated with Fatal Coronavirus
782   Disease, United States. *Emerg Infect Dis* **26**, 2005-2015, doi:10.3201/eid2609.202095 (2020).
783 65 Magro, C. *et al.* Complement associated microvascular injury and thrombosis in the pathogenesis of
784   severe COVID-19 infection: A report of five cases. *Translational Research* **220**, 1-13,
785   doi:10.1016/j.trsl.2020.04.007 (2020).
786 66 Haddock, E., Feldmann, F., Shupert, W. L. & Feldmann, H. Inactivation of SARS-CoV-2 Laboratory
787   Specimens. *Am J Trop Med Hyg*, doi:10.4269/ajtmh.21-0229 (2021).
788 67 Harcourt, J. *et al.* Severe Acute Respiratory Syndrome Coronavirus 2 from Patient with Coronavirus
789   Disease, United States. *Emerg Infect Dis* **26**, 1266-1273, doi:10.3201/eid2606.200516 (2020).
790 68 van Doremalen, N. *et al.* ChAdOx1 nCoV-19 vaccine prevents SARS-CoV-2 pneumonia in rhesus macaques.
791   *Nature* **586**, 578-582, doi:10.1038/s41586-020-2608-y (2020).

792 69   TW, H. B. & Girke, T. systemPipeR: NGS workflow and report generation environment. *BMC Bioinformatics*
793   **17**, 388, doi:10.1186/s12859-016-1241-0 (2016).
794 70   Zhou, Y. *et al.* Metascape provides a biologist-oriented resource for the analysis of systems-level datasets.
795   *Nat Commun* **10**, 1523, doi:10.1038/s41467-019-09234-6 (2019).
796